PCCP

Mechanism Behind the Photochromism and Photomagnetism of Biindenilidenediones type II: Multiconfigurational, Perturbative and Density Functional Theory Studies

Journal:	*Physical Chemistry Chemical Physics*
Manuscript ID	CP-ART-04-2021-001692.R2
Article Type:	Paper
Date Submitted by the Author:	24-Jun-2021
Complete List of Authors:	Castro, Pedro; Universidad del Atlantico, Faculty of Chemistry and Pharmacy Reguero, Mar; Universitat Rovira i Virgili, Química Física i Inorgànica

ARTICLE

Mechanism Behind the Photochromism and Photomagnetism of Biindenilidenediones type II: Multiconfigurational, Perturbative and Density Functional Theory Studies

Received 00th January 20xx,
Accepted 00th January 20xx

DOI: 10.1039/x0xx00000x

Pedro J. Castro*[a,b] and Mar Reguero[a]

Biindenylidenediones (BID) are a family of compounds that have been studied for a relatively short time. The crystals of these compounds are yellowish, and become purplish when they are irradiated and return back to their original color slowly in the dark or quickly when they are heated up. BIDs can be classified in different subfamilies depending on the nature of their substituents. BID-II crystals show a thermally dependent Electron Paramagnetic Resonance (EPR) signal that is a characteristic of chemical species with unpaired electrons. These properties make BIDs very attractive for industrial applications but the mechanisms responsible of their photocromism and photomagnetism are still under debate. In this article a computational study focused on the BID-II subfamily is presented. A variety of multiconfiguracional methods (CASSCF, CASPT2 and IDDCI) have been used to study exhaustively the topography of the potential energy surfaces of the lower electronic states of a single BID molecule. Methods based on Density Functional Theory (DFT) were then used to model the most important structures in a periodic crystal system. Our results suggest that δ-hydrogen abstraction could explain the observed experimental phenomena. After the initial excitation to the $^1\pi\pi^*$ state, non-symmetric $n\pi^*$ minima are populated, which are adiabatically connected with the photoproduct zone through a barrier along the reaction coordinate. Based on our set of results, we propose that an epoxide constitutes the most stable and accessible photoproduct preceded by the population of a triplet biradical of $\pi_O\pi^*$ nature which has only small geometrical differences in comparison with the reactant. The spin-orbit coupling indicates that the EPR signal arises due to the population of a low energy triplet through a thermally accessible intersystem crossing in the photoproduct zone.

Introduction

Nowadays, the photochromic compounds are the spotlight for researchers due to their potential applications in optical memories and photoswitches.[1,2] Among several families of organic photochromic compounds, biindenylidenediones (BID)[3] constitute a relatively new type reported for the first time by Tanaka and Toda in 1992.[4] This family has the peculiarity of exhibiting their photochromic properties only in crystalline state, a phenomenon called Aggregation Promoted-Photochromism (APPC).[5] Nevertheless, the most particular characteristic of BIDs is that their photochromism is accompanied by the formation of stable radicals that provide photomagnetic properties to the material (Aggregation Promoted-Photomagnetism, APPM). This is of particular importance due to its potential application in electronic devices development. Figure 1 shows the general structure of BIDs.

Owing to their molecular structure, BIDs have *cis-trans* isomerism regarding the relative position of the carbonyl groups. Besides, each *cis* or *trans* isomer has two additional isomers, *syn* and *anti*, depending on the position of the substituents with respect to the plane of the π system (Figure S1 of the ESI).

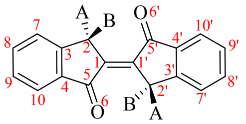

A = Aryl or Alkyl

B = Hydrogen o Hydroxyl

Type I: A = Aryl (Ar) B = Hydrogen (H)
Type II: A = Alkyl (R) B = Hydroxyl (OH)
Type III: A = Aryl (Ar) B = Hydroxyl (OH)
Type IV: A = Alkyl (R) B = Hydrogen (H)

Figure 1. General structure of BIDs and types according their substituents.

Photo-reactivity in solution is characterized by *cis-trans* isomerization due to the rotation around the central C_1-$C_{1'}$ bond. This reaction takes place without photochromism or photomagnetism.[6] Hence, the deactivation pathways leading to photochromism and photomagnetism are only important in a crystal lattice where the rotation around the central C_1-$C_{1'}$ bond is restricted due to the intermolecular interactions.[3] BIDs type I and II (BID-I and BID-II, respectively) have been the most studied ones. Up to now, the largest amount of synthetized derivatives

---

[a] Quantum Chemistry Group, Departament de Química Física i Inorgànica, Universitat Rovira i Virgili, 43007, Tarragona, Spain.
[b] Max Planck Researh Group, Facultad de Química y Farmacia, Universidad del Atlántico, Puerto Colombia, 081007, Colombia.
* pedrocastro@mail.uniatlantico.edu.co

Electronic Supplementary Information (ESI) available: [details of any supplementary information available should be included here]. See DOI: 10.1039/x0xx00000x has been reported for these two BID types.[6-27] Some derivatives belonging to type III have also been synthetized,[15-17] while there are no reports for the BID-IV type. The research groups of Koichi Tanaka and Ji-ben Meng have extensively studied BIDs. The first one has focused on the BID-I family, while the second has worked mainly with BID-II and BID-III types. Both of them have done important contributions via interpretations of the experimental data in order to gain a better understanding of the photochemical behavior of BIDs. Despite the structural differences among the systems investigated by the two groups, the experimental observations are similar for BID-I and BID-II types, indicating that the same mechanistic model should be expected to be applicable to both subfamilies. However, each research group has proposed a different mechanism to explain the phenomena observed experimentally creating a controversy.

Mechanism proposed to explain BID-I photoproperties

Tanaka and co-workers studied crystals of some *trans*(*syn*) isomers of BID-I type. These are yellow crystals that turn purple when they are irradiated with sunlight,[6] with the intensity of the photochromism depending on the solvent where the crystallization took place.[6-9] The irradiated crystals slowly return back to yellow in the dark, or very fast when they are heated. The irradiated crystals show an EPR signal characteristic of species with unpaired parallel electrons, suggesting that a triplet biradical is formed. In 2011,[10] Tanaka and co-workers, based on X-ray and IR findings, proposed that the mechanism responsible for the photochromism and photomagnetism is a γ-hydrogen abstraction (Norrish type II reaction) which implies considerable geometrical changes.[11] This reaction takes place via a triplet biradical intermediate,[12,13] which could explain the EPR signal (Figure 2).

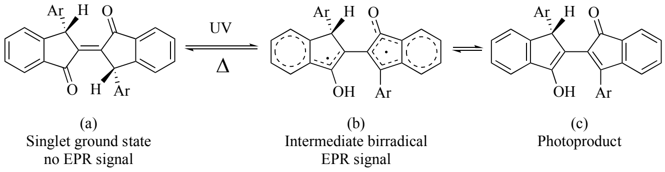

Figure 2. Photochromic mechanism proposed by Tanaka and co-workers.

This proposal could additionally explain the fact that the photochromism increases its life-time in the dark from 2h to 72h when the hydrogens on the *sp*^{3} carbons are replaced by deuterium.[14]

Mechanism proposed to explain BID-II photoproperties

In 2002[15,16] Meng and co-workers synthesized several BID-II. They showed that *trans*(*anti*) isomers have a more intense photochromism than *cis*(*syn*) isomers.[17,18] The photochromic crystals exhibit a temperature-dependent EPR signal. They observed that when the irradiated crystals are cooled at liquid nitrogen temperature, the EPR signal disappears without any change in color. However, this signal reappears as the temperature gradually increases to room temperature. It was also found that the hydrogens of the hydroxyl groups of the irradiated species lose their sharpness in the H^{1}NMR spectrum, which is associated with the increasing of H-O distances and subsequently weakening of the intramolecular hydrogen bond. A number of experiments were also carried out using substituent variations. The findings from those studies drove to conclude that the irradiated crystals are thermolabile biradical singlet species with antiferromagnetic properties, with a thermally accessible triplet.[19-27] Since no significant differences were observed in the IR and EPR spectra before and after irradiation, they proposed a mechanism mainly governed a by π–system rearrangement which does not involve any significant geometrical change or photochemical reaction (Figure 3).[3]

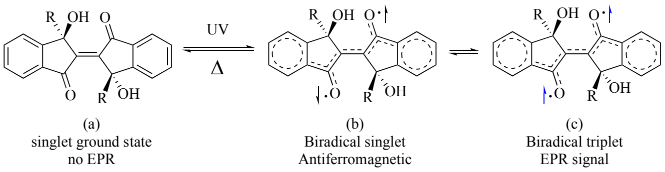

Figure 3. Photochromic mechanism proposed by Meng and co-workers.

Outline

Due to the potential application of BID and the scientific controversy about the species responsible of the phenomena experimentally observed, we have carried out a computational study to elucidate the mechanism involved in the photochemical properties of BID-II compounds. Both of the aforementioned mechanisms were investigated on a representative derivative of this family, using model systems for some computations. Our results were compared with the experimental evidences previously reported.

Computational Details

The representative member of the BID-II family chosen to develop this study is (3*R*,3'*S*,*E*)-3,3'-dihydroxy-3,3'-dipropyl-[2,2'-biindenylidene]-1,1'(3*H*,3'*H*)-dione, represented in Figure 4. To obtain accurate results in the study of the topography of the potential energy surfaces (PES) of the ground and excited states of this system, multireference computational methods must be used. Given the high computational cost of these methods and the size of the system of interest, a smaller system, labelled Model-1 (in red in Figure 4) was used for this part of our study. To test the suitability of this model to represent the full system, some representative results of this model were compared with those of a slightly simpler derivative of the full system, labelled Model-2, where the n-propyl substituents where replaced by methyl ones.

On the other hand, the calculations in crystal phase were performed using methods based on the Density Functional Theory (DFT). The lower computational cost of this methodology allowed the use of the full system in this part of the study.

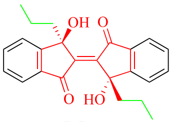

BID-II

Figure 4. Full system and models used along this work. In red: Model-1; in red+black: Model-2; in red+black+green: full system.

The computational strategy used in this work to explore the PES of the ground and low energy excited states of the model systems combines several multiconfigurational methods using the *d*-polarized split-valence basis set 6-31G(d).[28,29] This kind of calculations were ran on MOLCAS 7.6[30] and GAUSSIAN 09[31] packages.

The geometry optimization of the ground state and the lower excited states have been carried out using multiconfigurational self-consistent field (MCSCF) calculations of the complete active space (CAS) SCF class.[32] To study the smaller model system (Model-1), the wavefunction was obtained as a full configuration interaction expansion in an active space composed by 14 electrons in 12 orbitals. At some stages of the reaction, though, when the migration of a H atom is considered, the σ and σ^* orbitals of this bond should also be included in the active space. In these calculations we chose to exclude from the active space some "*irrelevant*" orbitals to keep an active space of tractable size (Figure S2 of the ESI).

Model-2 was studied using Restricted Active Space (RAS) SCF method where the active space was formed by 22 electrons (18 electrons from the π system and 4 from the lone-pairs of the carbonyl groups) in 18 orbitals. The RAS2 space was formed by 6 electrons in 5 orbitals, while the RAS1 and RAS3 were restricted to a maximum of 2 holes and 2 particles, respectively. Not symmetry restrictions were imposed unless the opposite is specified.

Once the stationary points were located at CAS/RAS SCF level, to incorporate the effect of the dynamic valence-electron correlation on the relative energies of the lower excited states we used the MCSCF wavefunction as reference to carry out both perturbative and variational methods. In the first case we used second-order multiconfigurational perturbation theory (CASPT2),[33,34] using the complete Fock matrix in the definition of the zero-order Hamiltonian and an imaginary level shift of 0.2 in order to avoid the incorporation of intruder states.[35] To allow the mixing between the reference state and one or more MCSCF states of the secondary space, we used the *Multi State* CASPT2 approach (MS-CASPT2). MS-CASPT2 approach uses a multidimensional reference space and constructs an effective Hamiltonian which is computed perturbatively, allowing the MCSCF states to interact via non diagonal terms. The eigenvalues of the effective Hamiltonian are the MS-CASPT2 energies while the eigenvectors give the *Perturbed Modified CAS Configuration Interaction* (PM-CAS-CI) functions (linear combinations of CASSCF states).[36]

To include the dynamic electron correlation via the variational principle, we used the iterative version of the Difference Dedicated Configuration Interaction method (IDDCI).[37,38] This is a multireference single and double configuration interaction (MRCI-SD) method that increases the configuration space by including selectively (based on quasi-degenerated PT2, QDPT2) single and double excited determinants with respect to each element of the CAS space.[37] The CAS space used in the IDDCI calculations was generated by 6 electrons in 4 orbitals. The initial molecular orbitals guess for the IDDCI calculations were obtained by averaging the singlet-SA3-CAS (SA3: state average of 3 states) and triplet-SA3-CAS molecular orbital sets on the given geometry. The DDCI space included 200 orbitals, resulting from freezing the *core* orbitals (8 and 12 for each irreducible representation for Model-1 and Model-2, respectively), and excluding 16 and 72 *virtual* orbitals for each irreducible representation for Model-1 and Model-2, respectively. Then, the density matrices obtained for each state from the DDCI calculations were averaged in order to obtain an averaged set of natural orbitals which was used in the next iteration until convergence. Finally, the Davidson correction (DC) was applied to the DDCI energies in order to decrease the typical size extensivity error resulting from truncating the CI space.[39]

Energy profiles based on linear interpolated and extrapolated internal coordinate (LIIC and LEIC respectively) paths were used to determine the topography of the low-lying excited states along the pathways linking the stationary points. Although minimum energy conical intersections (MECI) and intersystem crossings (ISC) can be located at the CASSCF level, when the energies are recalculated at the CASPT2 level, the degeneracy is lost due to the different contribution of the dynamic electron correlation for each state on the degeneration point. Therefore, the crossing points at the CASPT2 level were calculated via LIIC. As such, none of the crossing points presented in this work is a minimum energy point on the intersection space.

The spin-orbit coupling was calculated on the ISCs by calculating the matrix elements of the spin-orbit Hamiltonian ($\hat{H}^{SO}$) and its diagonalization using the RASSI module in MOLCAS 7.8. In addition, the oscillator strength for the excited states were also calculated using the CAS-state interaction method[40,41] (CASSI) in the same module.

In order to better reproduce the experimental conditions, the full system was modeled in the crystal phase with the use of periodic boundary conditions (PBC) in VASP 5.3.5 program,[42,43] taking as starting point reported experimental structures obtained by X-ray diffraction.[16] The energies in the crystal phase were calculated using DFT methods. The exchange and correlation energies were calculated using the Gradient Generalized Approximation via the PBE functional.[44,45] The *core* electrons were treated according to the projected augmented waves (PAW) of the Blöch method,[46] implemented by Kresse and Joubert.[47] The electronic density was approximated by using a set of plane waves with a 750 eV kinetic energy cutoff. The numerical integration of the reciprocal space was carried out using a 3×3×3 *k*-points Monkhorts-Pack mesh.[48] All geometries were optimized using the PBE functional in combination with the Grimme D2 dispersion correction,[49,50] and the optimization algorithm RMM-DIIS (*Residual Minimization Method – Direct Inversion in the Iterative Space*)[51] which is suggested by VASP's authors. The cell volume was optimized without changing the symmetry on each stationary point located.

Results and discussion

Gas phase

Franck-Condon (FC) zone and nature of the excited states. The models chosen to represent the BID-II family in gas phase have methyl and hydroxyl substituents linked to the sp^3 carbons. Despite having two chiral carbons, these systems are non-chiral (*meso* type) due to the symmetry point group (inversion center, C_i) of the ground state minimum energy geometry.

Due to the significant computational cost of the multiconfigurational methods, the complete computational study at this level was carried out for Model-1. To validate its use in representation of the full system, we first carried out a comparative study between Model-1 and Model-2.

Full geometry optimizations were carried out for both models. While for Model-2 the RASSCF(22,2,2;8,5,5) approach was applied using symmetry restrictions, for Model-1 the FC geometry was optimized with and without symmetry restrictions using CASSCF(14,12). The located stationary points are in very good agreement (Figure 5).

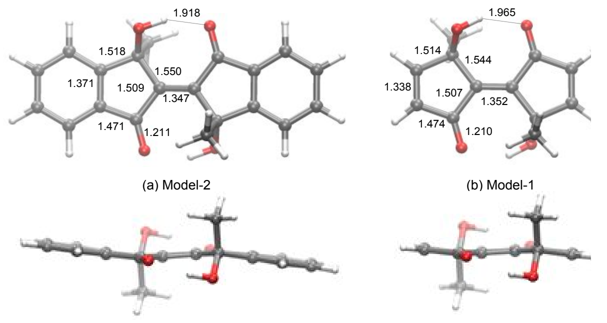

(a) Model-2 (b) Model-1

Figure 5. Minimum energy geometries for the ground state of: (a) Model-2 at RASSCF(22,2,2;8,5,5) level and (b) Model-1 at CASSCF(14,12) level.

Both minima have a pair of intramolecular hydrogen bonds where carbonyl and hydroxyl groups behave as acceptor and donor of hydrogen respectively. It is likely that this feature is responsible for the loss of planarity of these compounds. The excitation energies of the lower 6 singlets in the case of Model-2 and 10 for Model-1 were calculated and they are shown in Tables 1 and 2. In both cases the largest oscillator strength was obtained for the transition to the $^1\pi\pi^*$ excited state involving the π and π^* orbitals shown in Figure 6.

Although Model-2 has additional benzene rings, the most important molecular orbitals to describe the lower excited states are located in the common moieties with Model-1 (Figure 6). In addition, the weights of the main configurations describing the lower excited states are in very good agreement between the wavefunctions of Model-2 and Model-1. This suggests that the electronic density changes that take place during the electronic transitions in Model-1 must be very similar to the changes in Model-2. Tables 1 and 2 show that regardless of the model used, the lower excited states are described by singlets and triplets with $\pi\pi^*$ and $n\pi^*$ nature. It must be pointed out that the two equivalent n atomic orbitals are combined to form two molecular orbitals of A_g and A_u symmetry, labeled $n(A_g)$ and $n(A_u)$. Given the molecular symmetry and the small overlap of the n atomic orbitals, the $n(A_g)$ and $n(A_u)$ molecular orbitals are almost degenerated. The $n\pi^*$ states described by excitations from any of the n orbitals to the $\pi^*(A_g)$ show similar energies and changes in the molecular dipole moment because the electronic density changes are located in the same region of the space (Figure S3 of the ESI). The singlet and triplet described by excitations from $n(A_g)$ to $\pi^*(A_g)$ belong to the A_g irreducible representation, thus, they will be labeled as $(A_g)^{1,3}n\pi^*$ when we refer to both of them at the same time during the discussion. The same reasoning has been followed to label the singlet and triplet from $n(A_u)$ to $\pi^*(A_g)$, thus, they will be labeled as $(A_u)^{1,3}n\pi^*$ now and on.

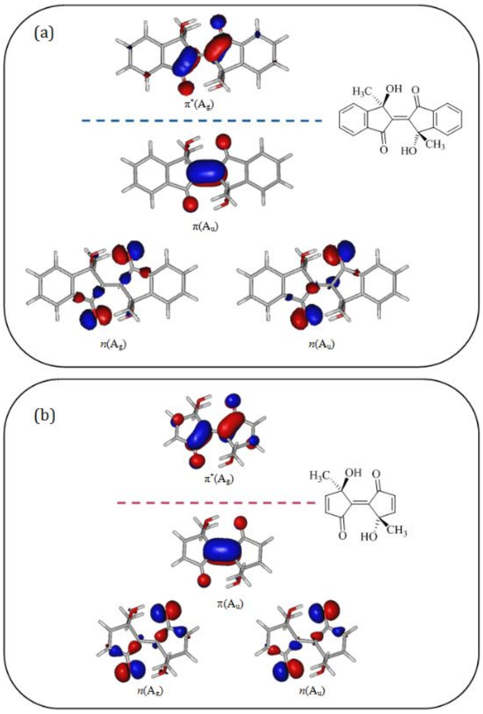

Figure 6. Singly occupied molecular orbitals in the dominant configurations that describe the lower excited states of Model-2 (a) and Model-1 (b).

As can be observed in Tables 1 and 2, for the $n\pi^*$ states of the same symmetry, the singlet-triplet energy gap is relatively small (around 4 kcal mol^{-1}), at CASSCF as well as at CASPT2 level. In contrast, the singlet and triplet $\pi\pi^*$ states are separated by very large energy gaps, of 82 and 86 kcal mol^{-1} for Model-2 and Model-1 at RASSCF and CASSCF level, respectively (Tables 1 and 2). Nevertheless, when the dynamic electron correlation is included, the $(A_u)^1\pi\pi^*$ is stabilized by 49 kcal mol^{-1} in Model-2 and by 35 kcal mol^{-1} in Model-1, whereas the $(A_u)^3\pi\pi^*$ is only stabilized by 6 and 1 kcal mol^{-1} for Model-2 and Model-1, respectively. The difference in the stabilization for the $(A_u)^1\pi\pi^*$ state in Model-2 and Model-1 can be explained by the additional configurations involving the two benzene rings taken into account in the perturbation terms in Model-2, but absent in Model-1.

Table 1. Nature and relative energies (in kcal mol^{-1}) of the lower singlet and triplet states at FC geometry for Model-2. Energies calculated at (a) SA6-RASSCF(22,2,2;8,5,5); (b) MS-RASPT2 and (c) IDDCI+DC levels.

Energies for Model-2					
Irred. Rep.	Nature	ΔE $^{(a)}$ (RASSCF)	ΔE $^{(b)}$ (MS-RASPT2)	ΔE $^{(c)}$ (IDDCI+DC)	$f^{(a)}$
A_g	$^3n\pi^*$	90.0 T_2	69.8 T_1	64.2 T_1	
	$^1n\pi^*$	93.5 S_1	75.4 S_1	64.0 S_1	0.00
A_u	$^3\pi\pi^*$	82.8 T_1	76.4 T_2	77.6 T_2	
	$^1\pi\pi^*$	165.0 S_8	116.0 S_5	77.7 S_2	0.35
A_u	$^3n\pi^*$	95.0 T_3	77.8 T_3	79.7 T_3	
	$^1n\pi^*$	97.8 S_2	82.9 S_2	80.1 S_3	0.00

Table 2. Nature and relative energies (in kcal mol^{-1}) of the lower singlet and triplet states at FC geometry for Model-1. Energies calculated at (a) SA10 and SA6-CASSCF(14,12) for singlets and triplets respectively; (b) MS-CASPT2 and (c) IDDCI+DC levels.

Energies for Model-1					
Irred. Rep.	Nature	ΔE $^{(a)}$ (CASSCF)	ΔE $^{(b)}$ (MS-RASPT2)	ΔE $^{(c)}$ (IDDCI+DC)	$f^{(a)}$
A_g	$^3n\pi^*$	87.9 T_2	74.5 T_1	70.6 T_1	
	$^1n\pi^*$	91.7 S_1	77.1 S_1	70.8 S_1	0.00
A_u	$^3\pi\pi^*$	77.3 T_1	78.2 T_2	81.2 T_2	
	$^1\pi\pi^*$	163.0 S_5	127.9 S_3	81.1 S_2	0.24
A_u	$^3n\pi^*$	90.8 T_3	81.0 T_3	86.5 T_3	
	$^1n\pi^*$	94.7 S_2	83.0 S_2	86.6 S_3	0.00

It is well known that the $\pi\pi^*$ states exhibit a larger singlet-triplet energy gap compared to the $n\pi^*$ states due to the overlapping of the singly occupied molecular orbitals. However, in this case, it is evident that the dynamic electron correlation is more important in the $(A_u)^1\pi\pi^*$ state, what subsequently leads to the decreasing of the singlet-triplet energy gap. It is also well known that when the perturbation correction in MRPT2 is very large, the error in the calculated energy can be large as well. Thus, to better calculate the energetics of the $(A_u)^1\pi\pi^*$ and $(A_u)^3\pi\pi^*$ states (labeled as $(A_u)^{1,3}\pi\pi^*$ to refer to both of them from now and on), the excitation energies were also calculated at the IDDCI+DC level, as shown in Tables 1 and 2. When the dynamic electron correlation is included in this way, it considerably affects the $(A_u)^1\pi\pi^*$ state, which is then almost degenerated with the $(A_u)^3\pi\pi^*$ and around 78 and 81 kcal mol^{-1} respectively in Model-2 and Model-1 above the ground state minimum. This leads to notably different results with respect to the RASPT2 and CASPT2 ones, where a large energy gap between the $(A_u)^{1,3}\pi\pi^*$ states was found (40 and 50 kcal mol^{-1} in Model-2 and Model-1, respectively). Regarding the other states computed, CASPT2 and DDCI-DC results are qualitatively similar.

As a whole, these results show that there is a good qualitative agreement for the excitation energies between Model-1 and Model-2, irrespective of the method used (Table S1 of the ESI). It can therefore be concluded that Model-1 can be used to describe the whole system, at least in the zone around Franck-Condon geometry.

The $n\pi^*$ excitation populates the antibonding π orbital of the carbonyl groups, leading the $n\pi^*$ states to decrease their energy as the C-O distances become larger. Two equivalent local minima labeled as Min-$^1n\pi^*(S_1)$ were located, characterized by a larger C-O distance on one carbonyl while the other one remains almost unchanged (Figure 8a). Despite the mirror-image geometries of these minima, their wavefunctions do not directly correlate, as it is shown in Figure 7, where the profile of the lower singlet PESs along the path that joins these minima with the FC geometry is depicted.

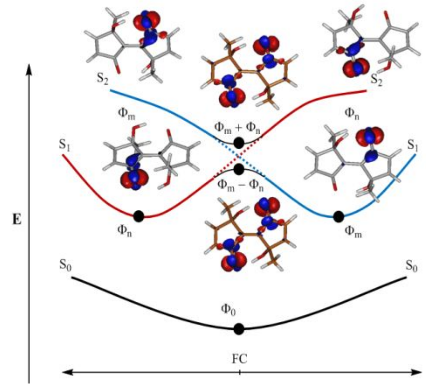

Figure 7. Representation, with data obtained at CASSCF(14,12) level (see Figure S5 of ESI), of the relationship between S_0, $^1n\pi^*(S_1)$ and $^1n\pi^*(S_2)$ states along the coordinate joining FC with the mirror-image Min-$^1n\pi^*(S_1)$ minima. Positive (blue) and negative (red) electronic density differences between the ground and $^1n\pi^*(S_1)$ and $^1n\pi^*(S_2)$ states at different geometries are also shown.

The $(A_g)n\pi^*$ and $(A_u)n\pi^*$ states found at FC geometry (S_1 and S_2) come from the linear combinations of two configurations Φ_n and Φ_m that describe localized excitations on one or another carbonyl group:

$$S_i = c_{mi}\Phi_{mi} \pm c_{ni}\Phi_{ni} \qquad \text{(Eq.1)}$$

At symmetric (C_i) geometries, the coefficients c_{mi} and c_{ni} have approximately the same absolute value, and form an avoided crossing at FC geometry. However, when the C-O distances symmetrically increase, the S_1-S_2 energy gap become smaller, reaching subsequently a symmetric conical intersection (Figure S4 of the ESI). On the other hand, when the symmetry is broken via the stretching of one of the two C-O distances, the coefficient of the configuration describing the excitation in that carbonyl increases, decreasing the energy of S_1 until the Min-$^1n\pi^*(S_1)$ minima, and increasing the S_1-S_2 energy gap. At these non-symmetric geometries, the S_1 and S_2 states cannot longer be classified as A_g or A_u (given that the molecule belongs to the C_1 point group) but, based on the Φ_{mi} and Φ_{ni} configurations, the correlation of states can be stablished, and this area of the PES can be viewed as an inversion of "*diabatic*" surfaces, that generates a double-well on S_1 (Figure 7). Keeping the symmetry constrained to the C_i point group, another critical point was located on S_1 (labeled Sym-$^{1}n\pi^{*}$(S_1), Figure 8b) that corresponds to a minimum energy point in this subspace, but it is in fact a transition state connecting the mirror-image minima of S_1 in the full space. On the other hand, a symmetric minimum of similar geometry was located on S_2 without any symmetry constraint. Contour plots of S_0, S_1 and S_2 can be found in Figure S5 and S6 of the ESI. The same behavior was observed for the optimization of the lowest energy triplet $n\pi^{*}$ surfaces, so the Min-$^{3}n\pi^{*}$(T_1) and Sym-$^{3}n\pi^{*}$(T_1) critical points were also located. The big similarity between Min-$^{1}n\pi^{*}$(S_1) and Min-$^{3}n\pi^{*}$(T_1) leads to the conclusion that the energetic behavior of these states is very similar despite the different multiplicities, at least, around the FC zone.

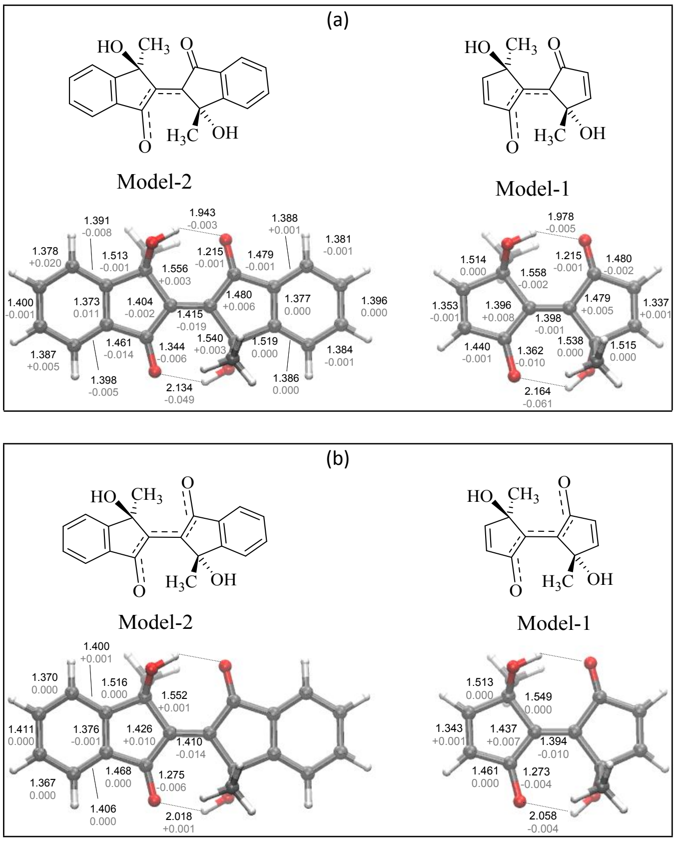

Figure 8. Stationary points located in the FC area on S_1 (distances in black) and T_1 (distance differences with respect to the singlet geometries in gray) at the CASSCF(14,12) level for the $^{1,3}n\pi^{*}$ states (a) Full optimizations, Min-$^{1,3}n\pi^{*}$(S_1/T_1) species. (b) Optimization constrained to C_i point group, Sym-$^{1,3}n\pi^{*}$(S_1/T_1) species.

Since the $(A_u)^{1}\pi\pi^{*}$ state is not well described at the CASSCF level, it is not possible to optimize this excited state. Despite this, the IDDCI+DC calculations showed that the $(A_u)^{1}\pi\pi^{*}$ is almost degenerated with the $(A_u)^{3}\pi\pi^{*}$ which unlike the $(A_u)^{1}\pi\pi^{*}$ is well described at the CASSCF level. The optimization of this triplet should lead to a good approximation of the Min-$(A_u)^{1}\pi\pi^{*}$ if it is not far from the FC geometry. The full optimization of the lowest $\pi\pi^{*}$ triplet state led to a minimum, labeled Min-$^{3}\pi\pi^{*}$(T_1) of C_i symmetry (Figure 9). This stationary point is mainly characterized by the stretching of the C-C central bond (+0.177 and +0.170 Å relative to the GS geometry, for Model-2 and Model-1, respectively). The existence of a similar minimum on the $^{1}\pi\pi^{*}$(S_1) state would explain the absence of phorochromism in solution, as the elongation of the C-C central bond favors the free rotation around this weakened bond, which leads to *cis-trans* isomerism, as observed experimentaly.[6] This kind of molecular change is prevented in the crystal lattice due to the packing and rigidness.

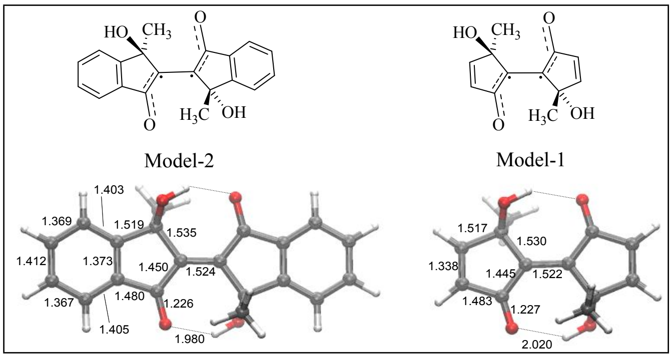

Figure 9. Minimum energy structure of the $(A_u)^{3}\pi\pi^{*}$(T_1) PES, located at CASSCF(14,12) level.

Table 3. Nature of the lower singlet and triplet states and excitation energies of several stationary points for Model-1 calculated at MS-CASPT2 level using SA3-CASSCF(14,12) wavefunctions.

State	FC	Min-$^{3}\pi\pi^{*}$(T_1)	Sym-$^{3}n\pi^{*}$(T_1)	Sym-$^{1}n\pi^{*}$(S_1)	Min-$^{3}n\pi^{*}$(T_1)	Min-$^{1}n\pi^{*}$(S_1)
S_0	0.0	13.0	5.7	7.2	16.8	17.4
$^{1}n\pi^{*}$	77.8	80.4	71.5	**71.5**	73.1	**73.1**
$^{3}n\pi^{*}$	73.6	78.4	**68.9**	69.2	**70.2**	69.8
$^{1}\pi\pi^{*}$	-	-	-	-	-	-
$^{3}\pi\pi^{*}$	78.4	**64.6**	71.4	71.0	74.2	74.8
$^{1}n\pi^{*}$	83.0	83.4	74.1	74.0	94.6	95.3
$^{3}n\pi^{*}$	79.6	81.7	72.1	72.0	96.8	98.2

Table 4. Nature of the lower singlet and triplet states and excitation energies of several stationary points for Model-2 and Model-1 calculated at IDDCI+DC level.

	FC		Min-$^{3}\pi\pi^{*}$(T_1)		Sym-$^{1}n\pi^{*}$(S_1)		Min-$^{1}n\pi^{*}$(S_1)		
Model	**2**	**1**	**2**	**1**	**2**	**1**	**2**$^{(a)}$	**1**$^{(a)}$	**1**
S_0	0.0	0.0	20.4	13.0	13.2	5.7	18.1	17.4	17.4
$^{1}n\pi^{*}$	64.0	70.8	74.6	73.1	**66.4**	**65.4**	**70.7**	**71.7**	**72.1**
$^{3}n\pi^{*}$	64.2	70.6	75.1	73.1	66.6	65.4	70.5	71.6	72.1
$^{1}\pi\pi^{*}$	77.7	81.1	**71.4**	**64.1**	78.0	71.5	80.6	79.9	80.2
$^{3}\pi\pi^{*}$	77.6	81.2	**71.5**	**64.2**	78.0	71.6	80.5	79.5	80.1
$^{1}n\pi^{*}$	80.1	86.6	84.3	82.2	76.0	73.7	-	-	85.5
$^{3}n\pi^{*}$	79.7	86.5	83.7	81.9	75.3	73.3	-	-	85.2

(a) Energies calculated using CAS(4,3) instead CAS(6,4).

To include the effect of the dynamic electron correlation on the energies of the stationary points located on the excited state PES in the vicinity of the FC geometry, CASPT2 and IDDCI+DC methods were used. Given that the DDCI method only gives accurate values for energy differences (whereas absolute energies are not meaningful), to obtain the excited state energies, the energy differences relative to the S_0 calculated at the IDDCI+DC level were added to the S_0 CASPT2 energy. The excited state energies recalculated are shown in Table 3 (CASPT2 energies for Model-1) and Table 4 (IDDCI+DC energies for Model-1 and Model-2). These data allow us to compare CASPT2 with DDCI energies and Model-1 with Model-2 results.

In agreement with the topography of the PES described at CASSCF level, the Min-$n\pi^*$ mirror-image minima are lower in energy than the transition state that connects them, Sym-$n\pi^*$. However, the dynamic electron correlation affects differently to the energy of these stationary points, stabilizing preferentially (both at CASPT2 and IDDCI+DC level) the Sym-$n\pi^*$ structure, and making it lower in energy than the corresponding Min-$n\pi^*$. In Model-1, the energy difference at CASPT2 level is only 1.6 and 1.3 kcal mol^{-1} for singlet and triplet structures, while this energy difference increases to 6.7 kcal mol^{-1} at IDDCI+DC level. These results indicate that the PESs obtained in this way can only be used in a qualitative description of the system, what is enough for the purpose of this study but, if quantitative results were looked for, geometry optimizations at CASPT2 level should be performed.

Study of the mechanism proposed for BID-II subfamily (π-system rearrangement): primary processes. IDDCI+DC combined with CASPT2 results suggest that upon the initial excitation, the $(A_u)^1\pi\pi^*(S_2)$ state is populated. Then, the molecular geometry is relaxed without any barrier toward the Min-$^1\pi\pi^*$ minimum, located on S_1. If we assume that the $^1\pi\pi^*$ state has its minimum close to the $^3\pi\pi^*$ one, the relaxation energy is approximately 6.3 and 17.0 kcal mol^{-1} for Model-2 and Model-1, respectively (Figure 10).

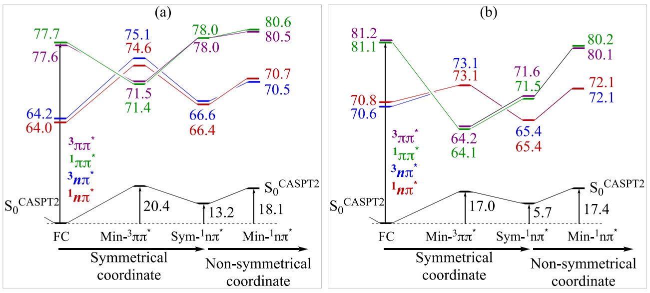

Figure 10. Relative energies (in kcal mol^{-1}) of the more significant stationary points, optimized at CASSCF level, in the neighborhood of FC geometry of the lower singlet and triplet states for (a) Model-2 and (b) Model-1. Values in red, blue, purple and green are vertical energies obtained by adding the energy differences calculated at IDDCI+DC level to the relative energies of the ground state minimum at CASPT2 level (in black). More information in Figure S7 of ESI.

As the relaxation takes place from FC-S_2 to the Min-$^1\pi\pi^*$ located on the S_1 PES, a S_1/S_2 crossing must have taken place along the path. Given that it runs along C_i structures, the crossing between the $n\pi^*$ and $\pi\pi^*$ PESs will be a real one, because the interaction between these states of A_u and A_g symmetry is null. The proximity in geometry and energy of the minima of the $^{1,3}n\pi^*$ and $^3\pi\pi^*$ states makes probable the population of them all. According to the empirical El-Sayed rules,[12] considerable interaction between $^1\pi\pi^*$ and $^3n\pi^*$ states is expected, but not between $^1\pi\pi^*$ and $^3\pi\pi^*$. This indicates that the population transfer from $^1\pi\pi^*$ to $^3n\pi^*$ is possible. The $^3\pi\pi^*$ also can be populated either from $^3n\pi^*$ or $^1n\pi^*$ via IC or ISC, respectively. So, all the $^{1,3}n\pi^*$ and $^{1,3}\pi\pi^*$ states could be populated simultaneously. The time scales and proportions of population for the $^{1,3}n\pi^*$ and $^{1,3}\pi\pi^*$ states can only be established by dynamical studies. From a static point of view, the relative energies and molecular deformation required to reach the critical points give valuable information regarding the kinetic and thermodynamic factors that will determine the evolution of the system. To investigate them, a more detailed analysis of the interaction between states was performed.

Because of the poor description of the $^1\pi\pi^*$ at the CASPT2 level and based on our previous DDCI results that show that singlet and triplet PES of the same nature ($n\pi^*$ or $\pi\pi^*$) are parallel and almost degenerate, this study examined the internal conversion between $^3n\pi^*$ and $^3\pi\pi^*$, and assumed that these results could be extended to the $^1n\pi^*$ and $^1\pi\pi^*$ states. To evaluate the possible path of depopulation of the $\pi\pi^*$ minimum, we obtained first the energetic profile of the path connecting the $^3\pi\pi^*$ minima with the Sym-$^3n\pi^*$ structure, build by linear interpolation of internal coordinates (LIIC), for Model-1. This profile was calculated at CASPT2 and IDDCI+DC levels, (Figure 11) following for the later the strategy explained before.

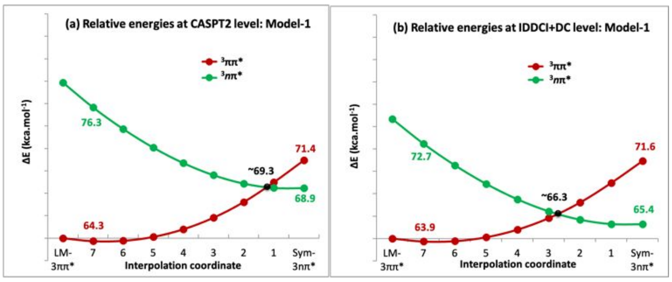

Figure 11. Energy profiles along LIIC between Sym-$^3n\pi^*(T_1)$ and LM-$^3\pi\pi^*(T_1)$ critical points for Model-1. Panel a: CASPT2 results. Panel b: CASPT2 curves vertically displaced according to the IDDCI+DC energies at the mentioned stationary points.

The results depicted in Figure 11 show that at IDDCI+DC level, the crossing point is very near the $\pi\pi^*$ minimum (only 2.1 kcal mol^{-1} higher), so from the energetic point of view it is easily accessible. Given that geometrically this crossing point is also very near the $\pi\pi^*$ minimum, it is expected that this area of the surface will be visited frequently. Any small deformation of the geometry breaking the symmetry will convert this real crossing into an avoided crossing, allowing the population of the $n\pi$ state. If this happens, the Sym-$n\pi^*$ and the mirror-image Min-$n\pi^*$ minima could be populated, and an equilibrium between $\pi\pi$ and $n\pi$ species would be stablished, although displaced towards the species thermodynamically favored. The energetics shown in Figure 10 indicates that this equilibrium will be displaced towards the $n\pi^*$ species in the case of Model-2, so it is expected that this will be also the case for the real system. To analyze the interaction in the FC area between surfaces of different spin, the effective spin-orbit Hamiltonian ($\hat{H}^{SO}$) was constructed on the basis generated by the MS-CASPT2 singlet and triplet states, allowing their coupling via non-diagonal terms (H_{ij}^{SO}). The eigenvalues of the spin-orbit Hamiltonian give the energies corrected by the spin-orbit coupling effect, while the eigenvectors provide the spin-orbit states (Φ_i^{SO}) which are a mixture of spin-pure states (in this case a mixture of singlets and triplets). At geometries far away from degeneracy areas, the spin-orbit states are almost pure MS-CASPT2 states, but if the energy difference becomes smaller, the spin-orbit effect can become stronger and the pure spin MS-CASPT2 states mix, generating the states Φ_i^{SO} and Φ_j^{SO} which have no pure spin. Usually, the spin orbit coupling is small in organic molecules, but relatively large for transition metals complexes.

We performed this analysis for Model-1. First, we focused on the interaction of the $^1n\pi^*$ state with the m_s=0 component of the $^3\pi\pi^*$ state. Our calculations on the $^1n\pi^*/^3\pi\pi^*$ crossing point showed that Φ_i^{SO} has 55% and 45% contributions of the (MS-CASPT2) $^1n\pi^*$ and $^3\pi\pi^*$ states respectively, while the Φ_j^{SO} state has inverted contributions. The coupling of states of different multiplicity is thus evident. The off-diagonal elements H_{ij}^{SO} of the spin-orbit Hamiltonian between the $^1n\pi^*$ and $^3\pi\pi^*$ states were not significant, thus, the singlet-triplet splitting generated is of only 2.0 cm^{-1}. These results suggest that the singlet-triplet coupling allows the interconversion between the $^1n\pi^*$ and $^3\pi\pi^*$ states, but due to the very weak avoided crossing generated (2.0 cm^{-1}), the population transfer will mostly take place only in geometries belonging to the intersection space.

We also calculated the effect of the spin-orbit coupling between the $^1n\pi^*$ and $^3n\pi^*$ states at the $^1n\pi^*/^3n\pi^*$ crossing point. Our results showed that the Φ_i^{SO} state is formed by 79% and 21% contributions of the (MS-CASPT2) $^1n\pi^*$ and $^3n\pi^*$ states respectively. A lower coupling compared to that of the $^1n\pi^*/^3\pi\pi^*$ crossing point was observed in this case, which is in agreement with the El-Sayed rules. The off-diagonal elements H_{ij}^{SO} for these states were not significant, so the singlet-triplet splitting is only 1.8 cm^{-1}. These results indicate that ISC can take place only in the intersection space, suggesting that this process cannot compete with internal conversion.

As a whole, these results suggest that in the area neighboring the FC geometry an equilibrium between $\pi\pi^*$ and $n\pi^*$ intermediates can be stablished on the S_1 or T_1 surfaces. The analysis of the spin density of the $^3n\pi^*$ and $^3\pi\pi^*$ structures of the different stationary points discussed so far (Figure S8 of the ESI) show that the only species characterized by well localized spin density on the oxygen atoms is the Sym-$^3n\pi^*$(T_1). Given that is structure is assumed to correspond in fact to a transition state, it is not expected to be populated long enough to give place to the EPR signal observed experimentally. Therefore, our computational results do not support the hypothesis of the existence of a thermally accessible triplet formed by π–system rearrangement without significant geometrical change, as proposed by Meng's group.[3] Moreover, given that there is not experimental evidence of fluorescence or phosphorescence, a non-adiabatic deactivation pathway from the S_1 and T_1 towards the ground state must exist.

Study of the mechanism proposed for the BID-I subfamily (Norrish type II reaction): secondary processes. The mechanisms proposed by Tanaka and co-workers to explain the photochromism and photomagnetism on BID-I was a Norrish type II reaction. Although this reaction involves most commonly a γ-hydrogen abstraction, when there is not an available γ-hydrogen it can also take place from the δ, β or even the ε-position (usually from δ),[53,54] depending on the conformational and steric availability of the hydrogen on the alternative positions.[11] This is the case of the BID-II subfamily, where the hydrogen abstraction is expected to take place from the only available position, the δ one. Therefore, we studied a Norrish type II reaction considering δ-hydrogen abstraction for Model-1. In this system, both the alkyl and hydroxyl groups have δ-hydrogens, so both could migrate. Given that some experimental results showed that BID-III also exhibit photochromism and photomagnetism[20] despite that they have hydroxyl groups and none alkyl groups, in the current study we have only considered the δ-hydrogen abstraction from the hydroxyl groups. This reaction implies the breaking of a $\sigma_{O\text{-}H}$ bond and the formation of a new $\sigma'_{O\text{-}H}$ bond, both localized in one of the sides of the BID, so the reaction path will run along non symmetric geometries. Moreover, due to the orientation of the O···H···O atoms involved in the reaction (see Figure 12), it is evident that the excited state that will favor this reaction will be the $n\pi^*$ one, and the precursor species of the reaction those in which the excitation is located in one of the hydroxyl groups (Min-$n\pi^*$). From the computational point of view, this situation implies that to study this step of our global reaction, we need to include in the active space the orbitals involved in the newly broken and formed σ bonds. The cartoon represented in Figure 12 shows that the *s* orbital of the migrating H atom and the *n*' orbital of the O' atom (being O' the oxygen of the hydroxyl group) should also be included in the active space. As already commented in the Computational Details sections, when including these orbitals in the active space, to avoid increasing its size, they will displace some irrelevant orbitals out of the active space (Figure S2 in ESI).

The Norrish type II reaction is therefore studied from the Min-$n\pi^*$ structure. According to the MS-CASPT2 LIIC shown in Figure S9 of the ESI, the energy barrier to go from Min-$^3n\pi^*$(T_1) to the product zone is equal or less than 9.2 kcal mol^{-1}. The maximum along this adiabatic connection is 79.4 kcal mol^{-1}, which is lower than the excitation energy at the same level of theory, thus, it is energetically accessible.

In the $^{1,3}n\pi^*$ states, the singly occupied *n* orbital becomes electrophilic so the strength of the hydrogen bond decreases, increasing its distance 0.2 Å relative to the FC geometry. However, the high spin-density (Figure S8 of the ESI) on the *n* orbital makes it more reactive, facilitating the homolytic cleavage of the O'-H bond to form a new O'-H hydroxyl group (being O the oxygen of the initial carbonyl group).

On top of the reaction mechanism explained up to here, it must be taken into account that at the Min-$^{1,3}n\pi^*$(S_1/T_1), the hydrogen bond is 34.6º above the plane of the carbonyl, so the overlap between the σ* orbital of the hydroxyl group and the π orbital of the carbonyl group is not negligible. This fact along with the high spin density of the π orbital (Figure S8 of the ESI) could trigger the σ bond formation between the migrating H and the *p* orbital of the carbonyl oxygen, as proposed if ref. 13, although this is expected to occur at a slower rate.

Once the hydrogen abstraction has taken place, in the area of the PES corresponding to the product of the Norrish II type reaction, the oxygen atom of the former hydroxyl group is left with a singly occupied *n*′ orbital and a doubly occupied p_O orbital. The energy of these atomic orbitals is very similar, giving place to two electronic distributions, $n'^1 p_O^2$ and $n'^2 p_O^1$ of similar energies (see Figure 12). Formally, these excited states can be described as single excitations to the π* orbital from a closed shell configuration where the oxygen atom of the former hydroxyl group would have four electrons in the *n*′ and p_O orbitals. According to this point of view, these excited states are labeled as $^{1,3}n'\pi^*$ and $^{1,3}p_O\pi^*$.

We located several stationary points on the S_0, S_1, T_1 and T_2 PES in the product zone using a (14,12) active space (shown in Figure S2c of the ESI). The closed shell configuration with four electrons in the *n*′ and p_O orbitals, that should be formally considered the ground state, is in this area high in energy, so all of the minima located in the lower energy PES correspond to species of biradical nature and their PESs are adiabatically connected with the $^{1,3}n\pi^*$ and $^{1,3}\pi\pi^*$ states of the FC zone.

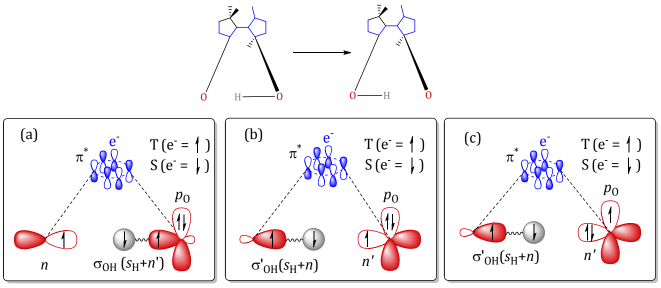

Figure 12. Representation of the orbitals and configurations involved in the hydrogen abstraction reaction. (a) $^{1,3}n\pi^*$ states before hydrogen abstraction. (b) and (c) $^{1,3}n'\pi^*$ and $^{1,3}p_O\pi^*$ states after hydrogen abstraction.

Two triplet minima were located, one on the T_1 and another one on the T_2 PES with $p_O\pi^*$ and $n'\pi^*$ nature, respectively. They are very similar to the FC geometry except for the migrated hydrogen which denotes that the reaction does not need a drastic rearrangement of the skeleton of the BID. These stationary points have been labeled as ^{3}P($p_O\pi^*$) and ^{3}I*($n'\pi^*$) where P and I* are the *product* and the *excited intermediate*, respectively. Their optimized geometries are shown in Figure 13. The ^{3}P($p_O\pi^*$) is located 64.8 kcal mol^{-1} higher than the S_0-FC and 5.4 kcal mol^{-1} lower than the Min-$^3n\pi^*$(T_1). On the other hand, the ^{3}I*($n'\pi^*$) is 70.5 kcal mol^{-1} higher than the S_0-FC and 0.3 kcal mol^{-1} higher than the Min-$^3n\pi^*$(T_1). This excited intermediate correlates with the $^3n\pi^*$ state in the FC zone and therefore, if the hydrogen abstraction takes place from the Min-$^3n\pi^*$(T_1), the ^{3}I*($n'\pi^*$) is expected to be initially populated. According to the energy profile for the T_1 along the coordinate connecting the Min-$^3n\pi^*$(T_1) and ^{3}P($p_O\pi^*$) species (Figure S9 of the ESI), the energy barrier for the hydrogen migration is equal to or less than 9.2 kcal mol^{-1}.

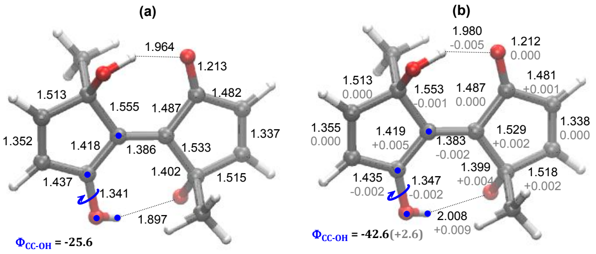

Figure 13. Optimized geometries at the CASSCF(14,12) level for: (a) the ^{3}P($p_O\pi^*$) and (b) the ^{1}I*($n'\pi^*$). The geometry of the triplet ^{3}I*($n'\pi^*$) species is shown in gray numbers, expressed as the difference with respect to the singlet.

With respect to the singlet states, the situation is more complex. The S_0 local minimum show $p_O\pi^*$ character, while the electronic nature of the local minimum on the S_1 PES (Figure 13b, black numbers) is an almost equally weighted mixture of the $p_O\pi^*$ and $n'\pi^*$ configurations so, as such, is labeled as ^{1}I*($p_O\pi^*$/$n'\pi^*$). This local minimum is 68.1 kcal mol^{-1} higher than the S_0-FC, so it is energetically between the T_1 and T_2 minima in the product zone (Table 5). When the profiles of the lowest energy PES were obtained at the CASPT2 level along the coordinate connecting the T_1 and T_2 minima, (Figure 14), it was found that at each end of the profile, the wavefunctions of the lowest singlet states are characterized by the predominance of only one electronic configuration, either $p_O\pi^*$ or $n'\pi^*$. In contrast, around the S_1 minimum energy geometry the wavefunctions acquire a stronger multiconfigurational character which is interpreted as a strong avoided crossing that generates the minimum located on the S_1 where the wavefunction results from a strong interaction of states

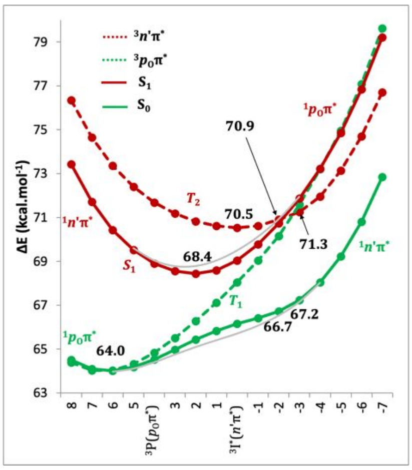

Figure 14. CASPT2 energy profile (in kcal mol^{-1}) for the S_0, T_1, S_1 and T_2 along the direction connecting the ^{3}P($p_O\pi^*$) and ^{3}I*($n'\pi^*$) stationary points. The MS-CASPT2 profiles for S_0 and S_1 are shown in gray.

As explained before, since the T_1 and T_2 keep the same electronic nature along the whole energy profiles, each triplet is described mainly by one dominant configuration. The energetic profiles of these PES plotted in Figure 14 show that there is a conical intersection between the $^{3}p_{O}\pi^{*}$ and $^{3}n'\pi^{*}$ states located very near the $^{3}I^{*}(n'\pi^{*})$ minimum on T_1 and only 0.7 kcal mol^{-1} higher than this stationary point. Therefore, if the $^{3}n'\pi^{*}$ state is populated after the hydrogen abstraction, an efficient internal conversion is expected to transfer the population to the $^{3}p_{O}\pi^{*}$ state which eventually is relaxed to the triplet product $^{3}P(p_{O}\pi^{*})$ on T_1.

Table 5. CASPT2 energies relative to the S_0-FC energy (in kcal mol^{-1}) of the stationary points located at CASSCF level in the product zone. The energies of the crossing points have been calculated as the average of the two states in the geometry with the lowest energy gap. The energy gaps at the crossing points are: (a) 0.35, (b) 0.18 and (c) 0.02 kcal mol^{-1}.

	$^{3}P(p_{O}\pi^{*})$	$^{3}I^{*}(n'\pi^{*})$	$^{1}I^{*}(p_{O}\pi^{*}/n'\pi^{*})$	$CI(T_2/T_1)$ $^{3}p_{O}\pi^{*}/^{3}n'\pi^{*}$	$ISC(T_2/S_1)$ $^{1}p_{O}\pi^{*}/^{3}n'\pi^{*}$	$ISC(T_2/S_1)$ $^{1}p_{O}\pi^{*}/^{3}p_{O}\pi^{*}$
S_0	64.53	66.16	67.47	67.24	66.72	68.05
T_1	64.83	68.04	68.26	71.42$^{(a)}$	70.14	71.95
S_1	68.90	69.05	68.10	71.87	70.82$^{(b)}$	73.21$^{(c)}$
T_2	71.68	70.53	70.86	71.42$^{(a)}$	70.82$^{(b)}$	73.21$^{(c)}$

In the surroundings of the $^{1}I^{*}(p_{O}\pi^{*}/n'\pi^{*})$ minimum, two intersystem crossings were also located. The analysis of their wavefunctions showed that the nature of these crossing points were $^{1}p_{O}\pi^{*}/^{3}n'\pi^{*}$ and $^{1}p_{O}\pi^{*}/^{3}p_{O}\pi^{*}$. The energies of these ISC were calculated including the spin-orbit coupling. The $ISC(^{1}p_{O}\pi^{*}/^{3}n'\pi^{*})$ showed to be 0.2 kcal mol^{-1} higher than the $^{1}I^{*}(p_{O}\pi^{*}/n'\pi^{*})$ S_1 minimum, so it can be reached almost at the same time than this minimum. At this point, the wavefunctions for $^{1}p_{O}\pi^{*}$ and $^{3}n'\pi^{*}$ are strongly mixed, with relative weights of around 50% (54.65 and 44.04% for the singlet and the triplet respectively at the lowest energy state). The off-diagonal elements in the spin-orbit Hamiltonian are 11, 11 and 25 cm^{-1}, the largest one corresponding to the triplet with m_s=0 and the singlet. After diagonalizing the $\hat{H}^{SO}$, the singlet-triplet energy gap became 58.71 cm^{-1}, which is considered to be very large for organic molecules. This means that there is a very strong spin-orbit coupling effect at this crossing, so a population transfer from the T_2 to S_1 with relatively large rate is expected. The second intersystem crossing, between the $^{1}p_{O}\pi^{*}$ and $^{3}p_{O}\pi^{*}$ states, is located 5.1 kcal mol^{-1} higher than the $^{1}I^{*}(p_{O}\pi^{*}/n'\pi^{*})$ S_1 minimum. At this point, the off-diagonal matrix elements of the $\hat{H}^{SO}$ are 5, 5 and 14 cm^{-1}, and the $^{1}p_{O}\pi^{*}$ and $^{3}p_{O}\pi^{*}$ wavefunctions are mixed in 58:42 proportion. The spin-orbit coupling effect generates a 31.75 cm^{-1} singlet-triplet energy gap, so a population transfer from the S_1 to the T_1 $^{3}(p_{O}\pi^{*})$ state is also expected. As a whole, these results indicate that the non-adiabatic processes on the $CI(^{3}p_{O}\pi^{*}/^{3}n'\pi^{*})$, $ISC(^{1}p_{O}\pi^{*}/^{3}n'\pi^{*})$ and $ISC(^{1}p_{O}\pi^{*}/^{3}p_{O}\pi^{*})$ points lead to the population of the $^{3}P(p_{O}\pi^{*})$ minimum, so we can assume that the system can spend considerable time on the triplet excited state in this zone of the nuclear configuration space, and thus, this long-lived triplet species could explain the EPR signal observed experimentally. Nevertheless, from the $^{3}P(p_{O}\pi^{*})$ minimum, a subsequent population transfer to the S_0 must take place, so we additionally studied the spin-orbit coupling between the T_1 and S_0 states, looked of an ISC between them and followed the relaxation path on the S_0 PES around the product zone. Figure 14 shows that at CASPT2 level the $^{3}P(p_{O}\pi^{*})$ minimum is displaced relative to the optimized geometry obtained at CASSCF level. At the minimum energy geometry of T_1 at CASPT2 level, this state is degenerated with S_0, of $^{1}p_{O}\pi^{*}$ character in this area, but the spin-orbit coupling between these states generates a splitting of 14 cm^{-1} and strong mixture (51:49 ratio) for the $^{1}p_{O}\pi^{*}$ and $^{3}p_{O}\pi^{*}$ wavefunctions. The population transfer would be slower than the one predicted at the $ISC(T_2/S_1)$ however, due to the fact that the crossing is located at the T_1 minimum and this state does not have a more accessible deactivation pathway, S_0 is expected to be populated via T_1.

Three minima were located in the product zone on the S_0 PES. The first one has $n'\pi^{*}$ character, but it shows a rotation around the C-OH bond, so the hydrogen moves away from its original position (Figure 15a). The analogue triplet minimum was also located. Although biradicals, these structures are stable products, so we labeled them as $^{1}P(n'\pi^{*})$ and $^{3}P(n'\pi^{*})$. However, it should be mentioned that, although located on the S_0 and T_1 PESs, they are 0.9 and 1.3 kcal mol^{-1} higher than the $^{1}I^{*}(p_{O}\pi^{*}/n'\pi^{*})$. The lowest energy S_0 minimum in the product zone is an epoxide obtained by the overlapping of the p_O and π^{*} orbitals that form a sigma bond between the O' oxygen and the nearest carbon of the C-C central bond. This is a closed shell stationary point located 34.1 kcal mol^{-1} higher than the S_0-FC, and it has been labeled $^{1}P(Epox)$. Its rotamer $^{1}P(EpoxRot)$ obtained by twisting around the C-OH bond was located as well, however, it was 3.5 kcal mol^{-1} higher in energy. At the $^{1}P(Epox)$ geometry, the two indenone fragments are twisted 56º around the C-C central bond. Since the real system is in a crystal lattice, it is possible that the rotation of two big moieties like indenone is restricted. Hence, we optimized the $^{1}P(Epox)$ constraining the torsion to an angle 8º larger than the one at FC geometry. The constrained $^{1}P(Epox)$ (Figure 15b) is located 38.8 kcal mol^{-1} higher than the S_0-FC and 26.0 kcal mol^{-1} lower than the triplet product $^{3}P(p_{O}\pi^{*})$.

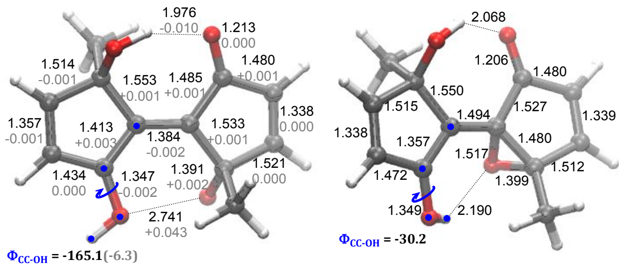

Figure 15. Geometries of Model-1 optimized at CASSCF(14,12) level in the product area on the lowest energy singlet and triplet surfaces: (a) $^{1}P(n'\pi^{*})$ and $^{3}P(n'\pi^{*})$ minima (in black, geometric parameters for the singlet; in gray, differences with respect to the singlet). (b) $^{1}P(Epox)$ minimum. Distances in angstroms and angles in degrees.

These results, calculated in gas phase, suggest that the $^{3}n\pi^{*}$ states are adiabatically connected to the product zone of the δ-hydrogen abstraction by overcoming a barrier below the excitation energy and equal to or less than 9.2 kcal mol^{-1} from Min-$^{3}n\pi^{*}(T_1)$. The $^{3}\pi\pi^{*}$ could also trigger this reaction, however, it must be a slower process. The $^{3}n\pi^{*}$ states connects, along the hydrogen migration coordinate, with the $^3n'\pi^*$ state, so the ^{3}I*($n'\pi^*$) minimum should be initially populated in the product zone. Once the ^{3}I*($n'\pi^*$) minimum is populated, very efficient non-adiabatic processes to the ^{1}I*($p_O\pi^*/n'\pi^*$) and the ^{3}P($p_O\pi^*$) minima must take place, given that the last is the most stable triplet species in this area. But the ^{3}P($p_O\pi^*$) species is almost isoenergetic to the ^{1}P($p_O\pi^*$), located on S_0 and, given the small spin-orbit coupling (14 cm^{-1}) between them, a population transfer to the S_0 via the intersystem crossing T_1($p_O\pi^*$)/S_0 will take place. Nevertheless, this is only a local minimum so the relaxation along the S_0 will lead to a close shell product ^{1}P(*Epox*) where an epoxide has been formed and it is 26.0 kcal mol^{-1} lower than the triplet product ^{3}P($p_O\pi^*$).

This proposal explains most of the phenomena experimentally observed. In the X-ray diffraction studies performed by Meng and co-workers[16] for BID-II compounds, the irradiated crystals show diffuse ellipsoids for carbon and oxygen atoms. This could be explained by the existence of the long-lived ^{3}P($p_O\pi^*$) species, which maintain almost the same arrangement of the heavy atoms than the reactant, as show Figure 16 where the skeleton of the ^{3}P($p_O\pi^*$) and the FC geometry are compared. Given that conventional techniques of X-ray diffraction cannot detect hydrogen atoms, the hydrogen migration would not be detected. Furthermore, the NMR^{1}H spectra showed that the signal of the hydrogens of the hydroxyl groups lost their sharpness,[16] which could be explained by the splitting that this signal undergoes when the molecular symmetry is lost by the migration of one of the hydrogen atoms. Finally, the existence of the stable closed shell ground state product ^{1}P(*Epox*) could explain also satisfactorily the photochromism of BID-II.

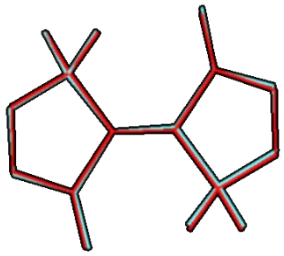

Figure 16. Superposition of the geometries of the S_0-FC and the ^{3}P($p_O\pi^*$) species showing only their heavy atoms (numerical comparison in Table S2 of ESI).

However, due to the large energy gap between the ^{1}P(*Epox*) singlet and the triplet biradical ^{3}P($p_O\pi^*$) intermediate, the thermal dependence of the EPR signal could not be explained. Given that one of the crudest approximations made in this study is to consider the system in gas phase, we recalculated in a crystal lattice the most crucial critical points that determine the photoproperties of BID-II in gas phase.

Crystalline phase

The unitary cell previously obtained experimentally for the full system was used as a starting point.[16] This compound, differently from Model-2, is characterized by *n*-propyl groups at the *sp*^{3} carbons (Figure 4). The unitary cell is a simple monoclinic crystal system which contains four molecules, that is 208 atoms. As it was explained in the Computational Details section, we used the DFT/PBE+D2 functional to study the crystal, so we focused on the lowest state for each relevant spin symmetry (in this case the S_0 and T_1) to explain BID's photoproperties.

To locate the critical points, the starting geometries were built using the skeleton of the structures obtained for Model-1 in gas phase. The FC, Sym-$^3n\pi^*$, ^{3}P($n'\pi^*$), ^{3}P($p_O\pi^*$), ^{1}P(*Epox*) and ^{1}P(*EpoxRot*) stationary points were located. It should be pointed out that the ^{3}P($p_O\pi^*$) could only be optimized imposing geometry constraints on the O-H bond distance of the newly formed hydroxyl group. The Min-$^3n\pi^*$ and Min-$^3\pi\pi^*$ could not be located, probably due to the fact that they are very close to the Sym-$^3n\pi^*$ one which must be lower in energy at this level of calculation. All optimized geometries are shown in Figure S10 of section II of ESI. The electronic nature of the T_1 species was identified using the spin densities which are shown in Figure S11 of the ESI. The relative energies for the stationary points are shown in Table 6 while in Figure 17 the energy profiles in the gas and crystal phases are illustrated.

Table 6. PBE+D2 relative energies (in kcal mol^{-1}) of the stationary points found in crystal phase.

	^{3}P($p_O\pi^*$)	^{3}I*($n'\pi^*$)	^{1}I*($p_O\pi^*/n'\pi^*$)	CI(T_2/T_1) $^3p_O\pi^*/^3n'\pi^*$	ISC(T_2/S_1) $^1p_O\pi^*/^3n'\pi^*$	ISC(T_2/S_1) $^1p_O\pi^*/^3p_O\pi^*$
S_0	64.53	66.16	67.47	67.24	66.72	68.05
T_1	64.83	68.04	68.26	71.42$^{(a)}$	70.14	71.95
S_1	68.90	69.05	68.10	71.87	70.82$^{(b)}$	73.21$^{(c)}$
T_2	71.68	70.53	70.86	71.42$^{(a)}$	70.82$^{(b)}$	73.21$^{(c)}$

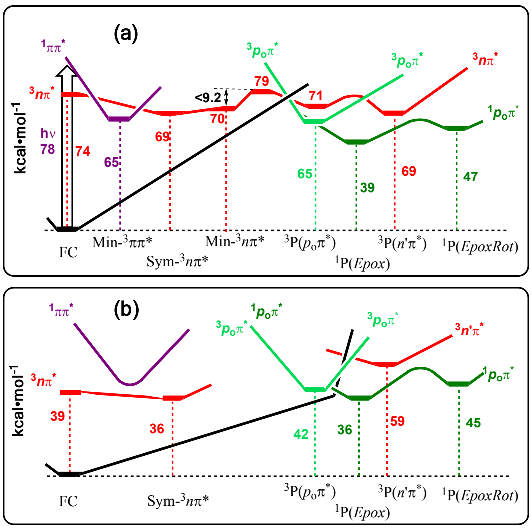

Figure 17. Potential energy surfaces according to: (a) CASPT2 results for Model-1 in gas phase, and (b) PBE+D2 results for the full system in crystal phase. Horizontal lines correspond to optimized structures, while curves correspond to inferred ones (without energies).

The green plain line represents the S_0 state in the product zone. It can be seen that there is a general high similarity between the results in gas and crystal phase. Nevertheless, the triplet states in the crystal phase show energies significantly lower than the ones obtained in gas phase. Therefore, the ^{3}P($p_O\pi^*$) strongly decreases its energy, getting close to the ^{1}P(*Epox*). In fact, while in Model-1, the energy difference between the singlet and triplet product is 26 kcal mol^{-1}, in crystal phase it is only 6 kcal mol^{-1} even for a ^{3}P($p_O\pi^*$) structure which has been optimized under geometry constrains. These results could explain the temperature dependence of the EPR signal: while the irradiated crystals are at room temperature, there is enough thermal energy to keep a significant population of the ^{3}P($p_O\pi^*$) minimum and the EPR signal is observed. On the other hand, when the system is cooled at liquid nitrogen temperature, the only minimum populated is the one of the ^{1}P(*Epox*) species because it is thermodynamically more stable, so the EPR signal disappears but, if the temperature increases, the triplet gradually restores its population and the EPR signal is recovered as well.

Conclusions

The mechanism behind the photochromism and photomagnetism in biindenylidenediones type II (BID-II) has been studied in gas phase using model systems and CASSCF/CASPT2 calculations, and in crystal phase using DFT calculations for the real system. The results obtained increase our current understanding of the possible events taking place on excited states and provide enough information to rationalize the photoactive behavior of the BID-II family of compounds.

Our results suggest that in the FC area there are singlet and triplet minima of $\pi\pi^*$ and $n\pi^*$ nature which geometries do not differ much from the ground state reactant geometry. After the initial excitation that brings the system to the $^1\pi\pi^*$(S_2) state, all these excited minima can be populated due to their large energetic and geometrical similarities which generate fully accessible intersection spaces for both internal conversion and intersystem crossing. Since the $n\pi^*$ triplet can be populated, species with a well localized spin density on the oxygen atoms, as stated in the Meng's hypothesis, exists; however, their population is expected to be small because they correspond to short lived intermediates. Therefore, we conclude that these $^3n\pi^*$ species are not the one responsible for the EPR signal observed experimentally.

On the other hand, the experimental findings can be explained by a Norrish type II reaction. Unlike the γ-hydrogen abstraction proposed by Tanaka and co-workers, we concluded that the population of the non-symmetric $n\pi^*$ minima (with the excitation localized in one of the carboxyl groups of the BID-II compounds) could trigger a δ-hydrogen abstraction from the hydroxyl groups leading to a birradical species on the S_1 or T_1 PES with no significant geometrical changes with respect to the FC geometry, with the exception of the migrated hydrogen. In this zone of the PES there is a considerably large spin-orbit coupling between triplet and singlet excited states which allows the eventual population of T_1 species of $p_O\pi^*$ nature which is stable enough to have a lifetime relatively long. In gas phase this species is significantly more energetic than the singlet epoxide photoproduct, which can be formed from the $^1p_O\pi^*$ intermediate, but in a crystal lattice the energy difference between the biradical $^3p_O\pi^*$ and the S_0 epoxide is small enough to allow a temperature dependent equilibrium between them, explaining the experimentally observed temperature dependency of the EPR signal.

The mechanism drawn from our results, that explain the experimental observations, can be schematize as shown in Scheme 1.

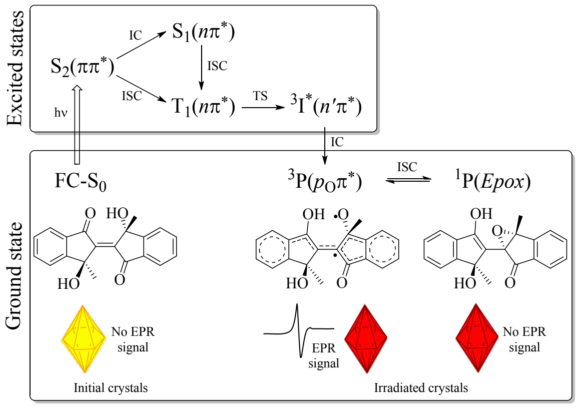

Scheme 1

Author Contributions

Prof Mar Reguero conceived the research idea, supervised the project and contributed to the data analysis via discussion with Dr Castro, who performed all the calculations, data analysis, defined the methodology, and wrote the manuscript. Both authors read, reviewed and approved this manuscript.

Conflicts of interest

There are no conflicts to declare.

Acknowledgements

Financial support has been provided by the Spanish Ministerio de Ciencia e Innovación (Projects HI04-337 and CTQ2017-83566-P) and the Generalitat de Catalunya (Project and Xarxa d'R+D+I en Química Teòrica i Computacional, XRQTC).

References

1 K. Matsuda, M. Irie. *J.Photoch. Photobio. C.* 2004**,** *5(2)*, 169.
2 B. L. Feringa. *Molecular Switches*, Wiley-VCH Verlag GmbH, New York*,* 2001**.**
3 J. Han, J. Meng. *J. Photoch. Photobio. C: Photochem. Rev,* 2009, *10*, 141.
4 K. Tanaka, F. Toda, T. Higuchi. *Mol. Cryst. Liq. Cryst,* 199, *219*, 135.
5 Z. He, L. Shan, J. Mei, H. Wang, J. W. Y. Lam, H. H. Y. Sung, I. D. Williams, X. Gu, Q. Miao and B. Z. Tang. *Chem. Sci.*, 2015, 6, 3538.
6 K. Tanaka, F. Toda. *J. Chem. Soc. Perkin Trans.* 2000, *1*, 873.X.

7 Li. *Journal of Chemical Research*, 2015, 39, 343.

8 K. Tanaka, Y. Yamammoto, S. Ohba. *ChemComm.* 2003, 1866.

9 K. Tanaka, Y. Yamamotoa, M. R. Caira. *CrystEngComm*, 2004, *6(2)*, 1.

10 K. Fujii, K. Aruga, A. Sekine, H. Uekusa, K. Sohno, K. Tanaka. *CrystEngComm.* 2011, *13*, 731.

11 N. Turro, V. Ramamurthy, J.C. Scaiano. *Modern Molecular Photochemistry of Organic Molecules*. University Science Books, Sausalito, California, 2010, 652.

12 M.A. El-Sayed, *Office of Naval Research*, 1968**,** Contact nonr-4756(07). Task No. NR 015-816.

13 C. D. DeBoer, W. G. Herkstroeter, A. P. Marchetti, A. G. Schultz, and R. H. Schlessinger. *J. Am. Chem. Soc.* 1973, 95(12), 3963.

14 K. Tanaka, Y. Yamamoto, H. Takano, M. R. Caira. *Chem. Lett.* 2003*, 32(8)*, 680.

15 L. Xu, J. Meng, H. Wang, P. Li, T. Sugiyama, Y. Wang. T. Matsuura. *Mol. Cryst. Liq. Cryst.* 2002, 389, 33.

16 L. Xu, T. Sugiyama, H. Huang, Z. Song, J. Meng, T. Matsuura. *ChemComm.* 2002, 2328-2329.

17 J. Han, Y. Wei, F. Zhang, J. Liu, M. Pang, J. Meng. *Journal of Molecular Structure,* 2009, 920, 23.

18 Chen, Y., Pang, M., Cheng, K., Wang, Y., Meng, J. *Chin. J. Chem*. 2012, 30, 1759.

19 L. Xu, J. Han, M. Pang, K. Cheng, Z. He, J. Meng. *Journal of Molecular Structure,* 2007, *874*, 28.

20 L. Xu, J. Han, M. Pang, Y. Cheng, J. X. Zhang, H. Ma, Z. He, J. Meng. *Tetra. Lett.* 2007, 48, 6044.

21 Y. Chen, M. Pang, K. Cheng, Y. Wang, J. Han, J. Meng. *J. Photoch. Photobio. A: Chemistry*, 2008, 194, 122.

22 Y. Chen, M. Pang, K. Cheng, Y. Wang, J. Han, J. Meng.*Chin. J. Chem.* 2010, 28, 1240.

23 J. Liu, J. Han, Z. Song, Y. Wei, M. Pang, J. Meng. *J. Mol. Struc.* 2008, 891, 214.

24 J. Liu, J. Han, J. Wang, M. Pang, J. Meng. *Chin. J. Chem.* 2009, 27, 1839.

25 J. Liu, J. Han, Y. Wei, F. Yao, M. Pang, J. Meng. *Appl. Organometal. Chem,* 2008, 22, 319.

26 C. J. McAdam, B. H. Robinson, J. Simpson. *Organometallics* 2000, 19(18), 3644.

27 J. Gan, H. Tian, Z. Wang, K. Chen, J. Hill, P.A. Lane, M.D. Rahn, A.M. Fox, D.D.C. Bradley. *Journal of Organometallic Chemistry*, *645*, (**2002**), pp.168–175.

28 W. J. Herhe, R. Ditchfield, J. A. Pople. *J. Chem. Phys.* 1972, 56, 2257.

29 P. A. Harihan, J. A. Pople. *Theor. Chim. Acta* 1973, 28, 213.

30 F. Aquilante, L. Vico, N. Ferré, G. Ghigo, P. A. Malmqvist, P. Neogrády, T. B. Pedersen, M. Pitoňák, M. Reiher, B. O. Roos, L. Serrano-Andrés, M. Urban, V. Veryazov R. Lindh, *J. Comp. Chem*. 2010, 31, 224.

31 Gaussian 09, Revision A.02, M. J. Frisch, G. W. Trucks, H. B. Schlegel, G. E. Scuseria, M. A. Robb, J. R. Cheeseman, G. Scalmani, V. Barone, B. Mennucci, G. A. Petersson et al., Gaussian, Inc., Wallingford CT, 2009.

32 For a review, see: B. O. Roos. *Adv. Chem. Phys.* 1987, 69, 399.

33 K. Andersson, P. A. Malmqvist, B. O. Roos, K. Wolinski. *J. Phys. Chem*. 1990, 94, 5483.

34 K. Andersson, P. A. Malmqvist, B. O. Roos. *J. Chem. Phys*. 1992, 96, 1218.

35 B. O. Roos, K. Andersson, M. P. Fülscher, L. Serrano-Andrés, K. Pierloot, M. Merchán-Molina, *J. Mol. Struct. Theochem*, 1996, 388, 257.

36 J. Finley, P. A. Malmqvist, B. O. Roos, L. Serrano-Andrés, *Chem. Phys. Lett.* 1998, 288 299-306.

37 J. Miralles, O. Castell, R. Caballol and J. P. Malrieu. *Chem. Phys.* 1993, 172, 33.

38 V. M. Garcia, O. Castell, R. Caballol and J. P Malrieu. *Chem. Phys. Lett.* 1995, 238, 222.

39 J. Cabrero, R. Caballol and J. P Malrieu. *Mol. Phys.* 2002, 100(6), 919.

40 P. Å. Malmqvist. *Int. J. Quantum Chem*. 1986, 30, 479.

41 P. Å. Malmqvist, B. O. Roos. *Chem. Phys. Letters* 1989, 155, 189.

42 A. L. Hagstrom, L. I. Johansson, S. B. M. Hagstrom, A. Christensen. *J. Electron Spectrosc*. 1977, 11, 75.

43 S. Otani, S. Honma, T. Tanaka, Y. Ishizawa. *J. Cryst. Growth* 1983, 61, 1.

44 J. P. Perdew, K. A. Jackson, M. R. Pederson, D. J. Singh, C. Fiolhais. *Phys. Rev. B* 1992, 46, 6671.

45 J. P. Perdew, Y. Wang. *Phys. Rev. B* 1992, 45, 244.

46 P. E. Blöchl. *Phys. Rev. B* 1994, 50, 17953.

47 G. Kresse, D. Joubert. *Phys. Rev. B* 1999, 59, 1758.

48 H. J. Monkhorst, J. D. Pack. *Phys. Rev. B* 1976, 13, 5188.

49 S. Grimme, J. Antony, S. Ehrlich, and S. Krieg, *J. Chem. Phys.* 2010, 132, 154104.

50 S. Grimme, S. Ehrlich, and L. Goerigk, *J. Comp. Chem.* 2011, 32, 1456

51 D. M. Wood and A. Zunger, *J. Phys. A*, 1985, 1343.

52 P. Pulay, *Chem. Phys. Lett*. 1980, 73, 393.

53 P. J. Wagner. *Acc. Chem. Res.*, 1989, 22, 3.

54 J. S. McKennis, L. Brener, J. S. Ward, R. Pettit. *J. Amer. Chem. Soc.*, 1971, 93(19)*,* 4958.